JOURNAL OF PROPULSION AND POWER
Vol. 21, No. 2, March–April 2005

# Computational Model of the Freezing of Jet Fuel

Daniel L. Atkins* and Jamie S. Ervin†
*University of Dayton, Dayton, Ohio 45469-0210*
and
Amit Saxena‡
*CFD Research Corporation, Huntsville, Alabama 35805*

**A computational fluid dynamics model is developed that simulates the solidification of jet fuel due to freezing in a buoyancy-driven flow. Flow resistance caused by porous crystal structures that exist in liquid–solid regions is simulated through the use of a momentum resistance source term. Experiments are performed in which jet fuel samples are cooled below their pour point temperatures in an optical cell. Polarized light is used to record images during the freezing process. In addition, low-temperature properties of jet fuel samples are determined, using a differential scanning calorimeter, pycnometer, and a low-temperature viscometer. The validity of the simulations is demonstrated by comparing temperature and solid area measurements with predicted values for various thermal boundary conditions and fuel samples. Reasonable agreement between experiments and simulations is obtained. Thus, the modeling technique is useful for aircraft fuel system designers in the prediction of fuel tank hold-up.**

## Nomenclature

| | | |
|---|---|---|
| $C$ | = | morphology constant, $m^{-2}$ |
| $C_0$ | = | Kozeny pore geometry constant |
| $C^*$ | = | product $C\mu$, $kg/m^3 \cdot s$ |
| $c$ | = | specific heat, $J/kg \cdot K$ |
| $f_l$ | = | liquid mass fraction |
| $f_l^*$ | = | normalized liquid mass fraction |
| $f_{n-\text{alkane}}$ | = | % weight $n$–alkane |
| $f_s$ | = | solid mass fraction |
| $g$ | = | gravity constant, $m/s^2$ |
| $H$ | = | liquid and solid enthalpy, J/kg |
| $h$ | = | liquid enthalpy, J/kg |
| $h_{\text{ref}}$ | = | reference enthalpy for Boussinesq approximation at $T_L$, J/kg |
| $K$ | = | permeability, $m^2$ |
| $k$ | = | thermal conductivity, $W/m^2 \cdot K$ |
| $P$ | = | pressure, Pa |
| $T$ | = | temperature, K |
| $T_H$ | = | temperature at onset of solidification, K |
| $T_L$ | = | temperature at $n$–alkane phase change completion, K |
| $t$ | = | time, s |
| $\boldsymbol{u}$ | = | superficial velocity, m/s |
| $\boldsymbol{u}_l$ | = | actual velocity, m/s |
| $v$ | = | scalar velocity in $y$ direction, m/s |
| $w$ | = | scalar velocity in $z$ direction, m/s |
| $y, z$ | = | coordinate directions |
| $\beta$ | = | coefficient of thermal expansion, $K^{-1}$ |
| $\Delta H$ | = | latent heat, J/kg |
| $\Delta H_e$ | = | effective latent heat, J/kg |
| $\lambda$ | = | porosity |
| $\mu$ | = | absolute viscosity, $kg/m \cdot s$ |
| $\rho$ | = | density, $kg/m^3$ |
| $\Sigma$ | = | interstitial surface area of the pores per unit volume of porous material, $m^{-1}$ |
| $\tau$ | = | tortuosity (ratio of tortuous flow-path length to material length) |

Received 10 December 2003; revision received 30 March 2004; accepted for publication 19 April 2004. 

*Ph.D. candidate, Mechanical and Aerospace Engineering Department, 300 College Park.

†Professor, Energy and Environmental Engineering Division, Research Institute, 300 College Park. Associate Fellow AIAA.

‡Engineer, Technical Support, Software Division, 215 Wynn Drive, Suite 501; currently with ESI Group, 215 Wynn Drive, Suite 503.

## Introduction

JET fuel solidification must be considered when an aircraft flies at high altitudes (>14 km) or operates in arctic regions. Frozen fuel can remain trapped within tanks or obstruct flow by blocking fuel system components and, if unchecked, may result in the loss of human life and aircraft. The ability to simulate and predict jet fuel freezing is a necessary tool for fuel system designers. From a fundamental perspective, there has been much research using computational fluid dynamics (CFD) to simulate the freezing of mixtures. Unfortunately, the mixtures considered in past CFD simulations generally are much simpler in composition than jet fuel.[1,2] Studies of metal alloy solidification have demonstrated the difficulties of modeling mixtures of three compounds.[3] Moreover, many researchers believe that it is impossible to predict accurately the final solid properties of some well-known mixtures, such as iron alloys, which have been studied for centuries.[3] Jet fuel is a mixture of thousands of hydrocarbon compounds, and the compositions of individual jet fuel samples vary with refinery source. Moreover, solidified jet fuel consists of crystals composed of solid solutions of normal alkanes ($n$–alkanes) and phase change takes place over a temperature range as species precipitate from the liquid fuel. The authors believe there are no published jet fuel CFD solidification simulations with experimental verification and that this is due to the complexities of the multiphase transport involved and experimental difficulties. Moreover, numerical techniques to simulate simultaneously both the microscopic and macroscopic phenomena occurring during solidification of complex mixtures are believed to be in their infancy.

Previous techniques used to simulate jet fuel freezing have had significant limitations. A previous one-dimensional numerical model incorporating the freezing of jet fuel relied entirely on empirical hold-up data.[4] (Fuel frozen in tanks, unavailable for use, is referred to as hold-up.) An accurate extrapolation of the results of this one-dimensional model to more complex geometries and flow conditions is unlikely. A two-dimensional CFD model was also developed to predict the temperature in fuel tanks. However, a mixture of water and glycerin was used as a surrogate fuel, and the effects of solidification were represented by altering the viscosity of the mixture.[1,2] Glycerin was used due to the opaqueness of jet fuel at low temperature and safety considerations. However, the appropriateness of using glycerin to represent jet fuel is unclear. There have

been efforts to develop a thermodynamic model for the equilibrium-phase compositions during the freezing of jet fuel.[5] Although phase equilibrium models do not include flow and heat transfer effects, the thermodynamic modeling of the phase compositions of complex hydrocarbon mixtures remains an important avenue of fundamental research. In summary, the authors have not found previous CFD models of the freezing of jet fuel that include a detailed treatment of phase change. A large impediment to the simulation of jet fuel freezing has been the absence of published thermophysical properties of jet fuel at low temperatures. The primary objective of the present work is to develop a two-dimensional CFD model that uses measured fuel properties to predict the solidification of jet fuels within a buoyancy-driven flow. Buoyancy-driven flow is the dominate flow in many fuel tanks.

Early wing tank simulator studies led Leo and von Meerwall to conclude that optical techniques are ineffective as tools to study jet fuel solidification behavior due to poor optical properties at low temperatures.[6] In contrast, our recent work has shown that high-quality images of the freezing of jet fuel are possible with the use of polarized light.[7] The use of polarized light has shown that jet fuel freezing involves interactions between precipitating solids and flowing liquid. Flow visualization and temperature measurements within an optical cell were obtained to develop a better fundamental understanding of the freezing of jet fuel and to validate numerical simulations.

## Experimental

The fidelity of a computational simulation is assessed by comparing experimental measurements to predicted values. Here, the computational model should reasonably predict the temperature at any location and time within the cooled fuel. In addition, the model should predict the location of an advancing liquid–solid boundary. In the current research, images of the solidification front and temperature measurements within the low-temperature optical cell (Fig. 1) are recorded for different thermal boundary conditions. The optical cell ($88.9 \times 38.1$ mm) was fabricated from aluminum (6061) tubing and has a depth of 44.5 mm to establish the desired two-dimensional flow by minimizing heat transfer end effects. Copper block heat exchangers are clamped to opposite vertical sides of the cell to impose the desired surface temperatures. Temperature control is accomplished by the use of cryogenic solenoid valves, which meter the flow of liquid nitrogen into the copper blocks. Consequently, the resulting density differences within the fuel drive the flow within the cell. Calibrated (type T) thermocouples measure temperatures on the internal surfaces of the aluminum cell. Quartz windows permit illumination and image collection. Cross polarization eliminates light transmittance through the liquid fuel. As the fuel solidifies, crystals rotate the polarization plane and allow light to pass through the front polarization analyzer. Additional details of the low-temperature optical cell are given elsewhere.[7]

Samples of JP-8 (F3804) and Jet A (F3219) fuels and a Jet A fuel (F3219) mixed with 2000 mg/l of a proprietary low-temperature additive (F3607) were used. An additive mixture was included due to the potential commercial and military applications for additives that improve the low-temperature performance of Jet A and JP-8. The freeze-point [American Society for Testing and Materials (ASTM) D5972-96], cloud-point (ASTM D5773-95), and pour-point (ASTM D5949-96) temperatures of the fuel samples were measured using a Phase Technology Series 70V petroleum analyzer and are listed in Table 1. In addition, gas chromatography in combination with a mass spectrometer was used to determine the *n*–alkane (weight) distribution of the fuels. As already noted, *n*–alkane species are believed to be largely responsible for the freezing of jet fuel.

Solution of the governing equations requires low-temperature thermal properties of both liquid and solid jet fuel. Unfortunately, published properties of jet fuel at low temperatures, including density, viscosity, thermal conductivity, and specific heat are limited.[4,8] Moreover, they are generally unavailable for temperatures below 233 K. Jet fuel properties vary widely depending on their source, whereas model accuracy depends on accurate measurements of these properties. Thus, property measurement for use in low-temperature simulations is warranted.

The density of jet fuel samples varies with refinery source. However, Fig. 2 shows that, although the measured density of three samples (445, 168, F3804) of JP-8 fuel varies, the difference is small (<3%) (Ref. 4). Moreover, Fig. 2 shows that the densities of samples of JP-8 and Jet A fuel are similar and have been represented by an aggregate linear function of temperature for the liquid phase [Coordinating Research Council (CRC), Ref. 8]. In the present work,

**Table 1 Freeze point, cloud point, and pour point temperatures of jet fuel samples and phase change onset**

| Fuel | Freeze point, K (±0.5 K) | Cloud point, K (±1.0 K) | Pour point, K (±2.0 K) | Cell onset, K (±0.3 K) | DSC onset, K ±0.5 K |
|---|---|---|---|---|---|
| JP-8 (F3804) | 224.9 | 221.2 | 215.2 | 221.2 | 220.8 |
| Jet A (F3219) | 227.2 | 222.2 | 217.2 | 220.5 | 222.2 |
| Jet A (F3219) + additive (F3607) | 227.2 | 221.6 | 213.4 | 218.5 | 221.2 |

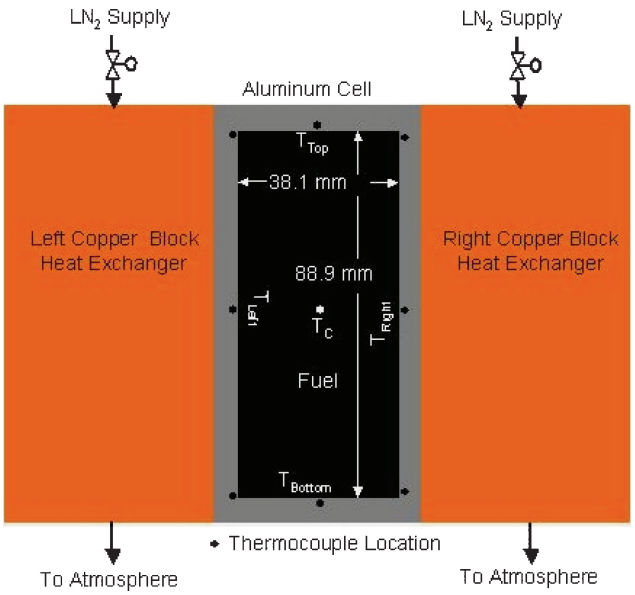


**Fig. 1 Schematic of low-temperature optical cell.**

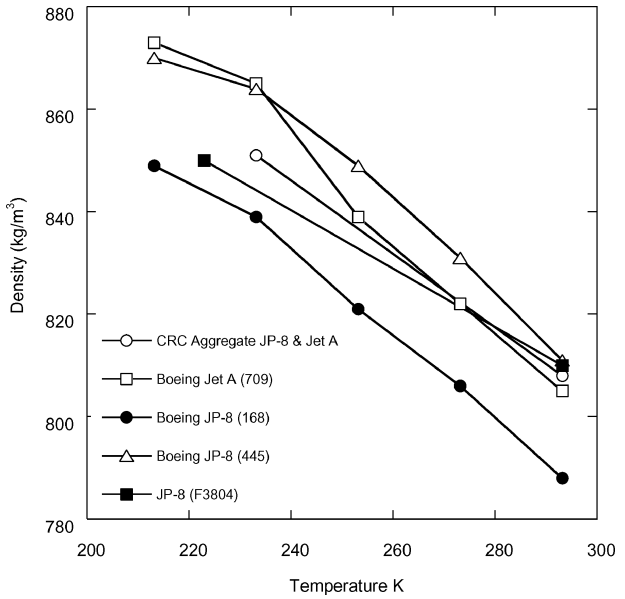


**Fig. 2 Jet fuel density for different fuel samples and temperatures.[4,8]**

the density of F3804 at 291.0 K was gravimetrically determined to be $810 \pm 1$ kg/m$^3$, and the density at the onset of phase change (221.2 K) was measured with a pycnometer as $849.2 \pm 0.5$ kg/m$^3$ (Ref. 9). Thus, the density of F3804 varies by less than 5% between 291.0 and 221.2 K. In addition, the densities of fuel samples F3219 and F3804 differed by 1% at 15°C. For simplicity, it is reasonable to assume that the densities of fuels F3804 and F3219 remain constant at 830 kg/m$^3$ except in the buoyancy source term (Boussinesq approximation) of the momentum equation. This density value is midway between the measured maximum and minimum density values for fuel F3804 in the temperature range of interest (208–291 K). During solidification, individual *n*–alkanes ($C_8$–$C_{17}$) that are commonly found in jet fuel increase in density by roughly 6% (Ref. 10). These *n*–alkanes represent a fraction (about 25%) of the total fuel mass. Consequently, it is reasonable to assume that changes in density due to freezing *n*–alkanes are essentially negligible for simulation purposes.

A rotational viscometer (Tannas Company, Model Plus Two) was used to measure the dynamic viscosity of the F3804 fuel sample for temperatures between 291.0 and 221.2 K. A polynomial fit of the measured viscosity as a function of temperature reasonably represents the measured viscosity and is, $\mu = 2.444 \times 10^{-9} T^4 - 2.675 \times 10^{-6} T^3 + 1.097 \times 10^{-3} T^2 - 1.999 \times 10^{-1} + 13.66$ kg/m · s (Fig. 3). For simplicity, liquid–solid mixture viscosity values below 221.2 K are assumed to follow extrapolation of the fit of Fig. 3 in simulations involving fuel F3804. Figure 3 shows a comparison of the polynomial fit with reported viscosities of Jet A and JP-8 fuels.[4,8] Our measurements agree well with the previously measured values from 291 to 240 K. However, below 240 K, Fig. 3 shows that there are substantial differences between the measured viscosity of F3804 and the viscosities of fuel samples measured in the earlier studies. These differences are not surprising because we have observed that differences in viscosity measurements among fuel samples from different refinery sources become larger as the cloud-point (onset of crystallization) temperatures of the individual samples are approached. There was little difference between the measured viscosities of fuels F3804 and F3219 over the temperature range of Fig. 3. Thus, the viscosity measured here for fuel F3804 was used in all simulations. Moreover, the authors believe, after comparing viscosity measurements to three lower freeze-point JP-8 fuels, that the freeze-point specification minimum JP-8 sample (F3804) may potentially be used to predict the maximum hold-up.

To the best of our knowledge, published values of jet fuel thermal conductivity at low temperatures (below 253 K) do not exist.

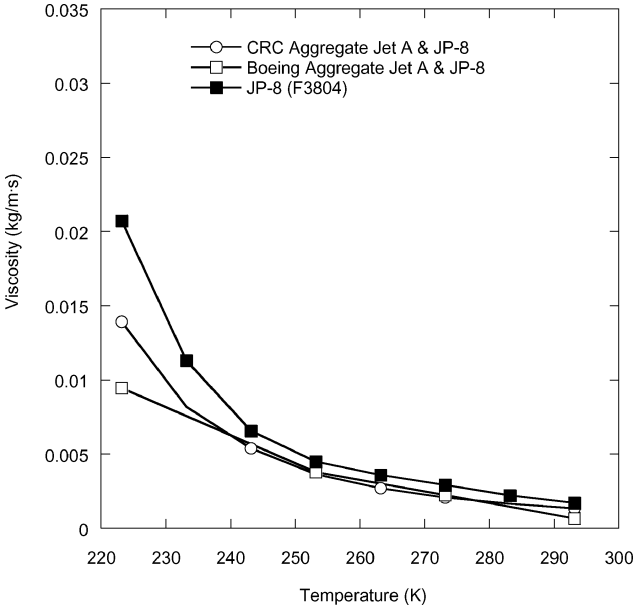


**Fig. 3 Absolute viscosity of JP-8 and Jet A fuels for different temperatures.[4,8]**

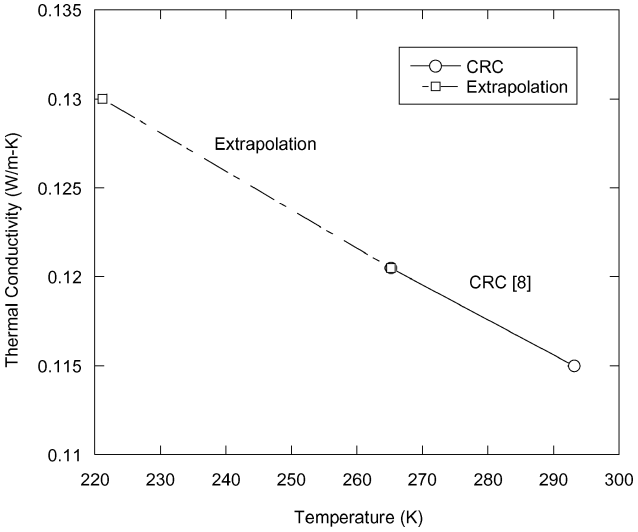


**Fig. 4 Thermal conductivity of Jet A and JP-8.**

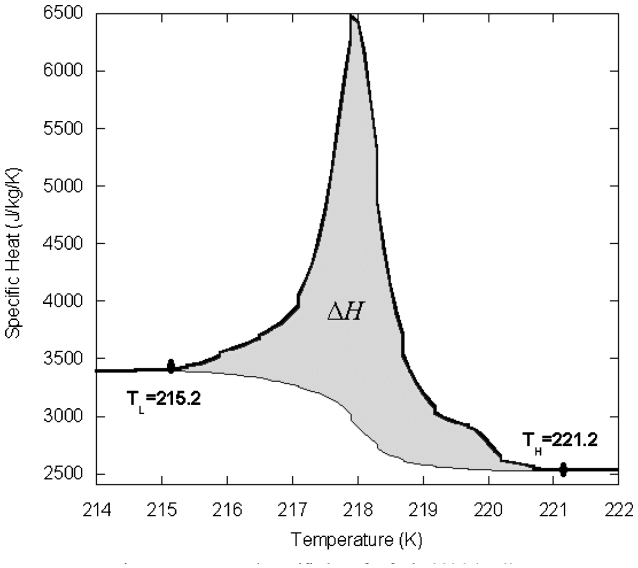


**Fig. 5 Measured specific heat for fuel F3804 (JP-8).**

Figure 4 shows that the thermal conductivity of liquid jet fuel varies linearly with temperature between 300 and 265 K (Ref. 8). Linear extrapolation to 221.2 K yields a value of approximately 0.13 W/m$^2$ · K for liquid jet fuel. This extrapolated value agrees well with thermal conductivity values of jet fuel *n*–alkane constituents, for example, tetradecane has a thermal conductivity of 0.1399 W/m$^2$ · K at the solidification temperature.[11] Thus, for simplicity, the thermal conductivity of the liquid jet fuel is assumed to be 0.12 W/m$^2$ · K at 291.0 K and increases linearly to 0.13 W/m$^2$ · K at 221.2 K in all simulations. The thermal conductivity of *n*–alkanes can increase by 25–50% upon crystallization.[12] Thus, for simplicity and the absence of thermal conductivity measurements, the thermal conductivity of the liquid–solid mixture below the solidification temperature (221.2 K for F3804 and 222.2 K for F3219) is assumed here to be 0.18 W/m$^2$ · K.

The differential scanning calorimeter (DSC) can be used to determine specific heat and enthalpy as functions of temperature as well as indicate phase transition temperatures. A DSC (TA Instruments Model 2920, cooling rate 1 K/min) was used to determine the effective specific heat and heat of fusion for solidifying constituents within the fuel samples (F3219 and F3804). Figure 5 shows that the measured specific heat (F3804) varies less than 3% until the onset of solidification (221.2 K) and is approximately 2500 J/kg · K. At 221.2 K ($T_H$, Fig. 5), the specific heat begins to increase due to

the onset of freezing within the hydrocarbon mixture. Additionally, Table 1 shows that temperatures measured at the onset of solidification, which was determined both visually in the optical cell and with the DSC, agree fairly well with the measured cloud-point temperatures. With continued cooling, the specific heat peaks, begins to decrease, and ultimately levels after the larger *n*–alkane constituents have solidified ($T_L$, Fig. 5). A similar procedure was followed for fuel F3219. The specific heat behavior during phase change varied significantly among the fuel samples. Thus, measured values of the specific heat obtained from the DSC for each fuel sample were used in the simulations. The JP-8 sample utilized represents a freeze-point specification minimum fuel, and the authors believe the measured thermal properties may potentially be used to predict the maximum hold-up.

## Simulation Methodology

In the current work, the freezing of jet fuel in the rectangular cavity of Fig. 1 is simulated using primitive variables. The cavity is long in the viewing direction, and thus, the flow is essentially two dimensional. In addition, the buoyancy-induced flow is laminar in our experiments. We assume that the liquid fuel itself behaves as a Newtonian fluid and that the density is constant in all terms except the buoyancy source term (Boussinesq approximation).

In our simulations, we employ an enthalpy method that has been used previously to simulate the solidification of simple mixtures in buoyancy-driven flows.[13] With the enthalpy method, the governing energy equation incorporates the heat of fusion due to phase change, and the heat of fusion must be accounted for on the advancing liquid–solid interface. The energy equation is written in terms of the liquid–solid enthalpy $H$,

$$H = h + \Delta H \tag{1}$$

In Eq. (1), $\Delta$H is the heat of fusion from solidifying constituents. The heat of fusion is incorporated over the entire liquid–solid region. Thus, the liquid and solid phases are not treated separately. Incorporating the heat of fusion enables a simple fixed grid to be used, avoiding the complexity of deforming grids that account for the moving liquid–solid interface. Such simplifications are advantageous for large computational domains as might be expected for simulations of an aircraft fuel tank. Admittedly, this enthalpy method has limitations.[3] For example, details of the microstructure of the fuel crystals cannot be predicted, and local thermodynamic equilibrium is invoked. However, such limitations are not considered fatal for the prediction of fuel tank hold-up and flow.

For complex mixtures, such as jet fuel, that solidify over a temperature range, porous structures form that resist flow. It is believed that freezing jet fuel forms a matrix of crystals, but the nature of the matrix is not understood.[7] A fixed grid formulation requires that a momentum exchange source term be added to the momentum equation to account for changes in velocity due to the added flow resistance. The flow rate through a porous material can be represented by the empirical D′Arcy[14] relation (also see Ref. 15),

$$\boldsymbol{u} = -(K\nabla P/\mu) \tag{2}$$

In Eq. (2), $\boldsymbol{u}$ is the superficial velocity (ensemble-average velocity), and is defined in terms of the porosity $\lambda$ and the actual fluid velocity $\boldsymbol{u}_l$

$$\boldsymbol{u} = \lambda \boldsymbol{u}_l \tag{3}$$

The permeability is a property of the porous material that characterizes the ease with which a fluid flows under a pressure gradient. $K$ is determined by pore geometry, which may, in reality, vary anisotropically and have a statistical distribution of sizes. Several empirical and semi-empirical representations for $K$ exist, and the Kozeny[16] relation is often invoked (also see Refs. 15 and 17),

$$K = C_0\lambda^3 \big/ \tau\Sigma^2 \tag{4}$$

In Eq. (4), $C_0$ is a dimensionless constant that depends on the pore geometry. The actual flowpath may likely be indirect. Thus, the tortuosity $\tau$, (ratio of tortuous flowpath length to material length) is sometimes included in Eq. (4)[15]:

$$K = C_0\lambda^3 \big/ \tau\Sigma^2 \tag{5}$$

In practice, $C_0$ is empirically determined, and measurements (if at all possible) of $\lambda$, $\Sigma$, and $\tau$ may have large uncertainties. Some researchers prefer a simpler expression,[13]

$$K = \lambda^3/C(1-\lambda)^2 \tag{6}$$

$C$ of Eq. (6) is an empirical constant that includes the effects of $\Sigma$ and $\tau$ together with the influence of pore shape, size, and orientation. For crystallization, $C$ is assumed to characterize the morphology of the porous medium and is hereafter referred to as the morphology constant. Equation (6) can be used with the D′Arcy relation to give an expression for the pressure gradient in the two-phase coexistence region:

$$\nabla P = -C\mu[(1-\lambda)^2/(\lambda^3)]\mathbf{u} \tag{7}$$

Equation (7) shows that as the porosity approaches unity (liquid alone), pressure loss due to flow through the porous media decreases to zero. As the porosity approaches zero, the pressure drop increases to eliminate flow within a region of liquid–solid coexistence. Moreover as $C$ is increased for a fixed $\mu$, $\lambda$, and velocity, Eq. (7) shows that the flow resistance increases. Thus for jet fuel, crystallization behaviors that inhibit flow would tend to have larger values of $C$.

Results from analytical phase-separation techniques[18] show that approximately 8% (mass) of the F3804 fuel sample actually solidifies at the minimum temperature of interest (215.2 K). As observed elsewhere, only a relatively small mass fraction of jet fuel solidifies, and this fraction consists essentially of *n*–alkanes.[5] Here, the mass fraction of fuel that becomes solid is referred to as $f_s$, and the mass fraction that remains liquid is $f_l$. Thus, for fuel sample F3804, the maximum value of $f_s$ is 0.08, which coincides with a minimum $f_l$ of 0.92. As *n*–alkanes precipitate from solution, $f_s$ increases while $f_l$, $\lambda$, and $K$ decrease. Unfortunately, $\lambda$ is difficult, if not impossible currently, to measure under the low-temperature conditions occurring with solidifying jet fuel. However, it is reasonable to assume that $f_l$ is proportional to $\lambda$, and as an approximation, $\lambda$ of Eq. (7) may be replaced with $f_l$,

$$K = f_l^3 \big/ C(1-f_l)^2 \tag{8}$$

For convenience, $f_l$ is normalized to vary between 0 and 1. Because there is a large uncertainty in $C$ of Eq. (8), the use of a normalized $f_l$ is acceptable. Here $f_l$ is a function of temperature and is estimated using DSC measurements for a particular jet fuel sample. (In the remainder of this paper, $f_l^*$ refers only to the normalized mass fraction of fuel that remains liquid. For simplicity, we also rename the product $C\mu$ [Eq. (7)] as $C^*$ using appropriate units.) The momentum equations for buoyancy-dominated flow through a region that may have *n*–alkane crystal structures include the momentum source terms and are written in terms of the superficial velocity,[13,19]

$$\frac{\partial(\rho v)}{\partial t} + \nabla\cdot(\rho\boldsymbol{u}v) = \nabla\cdot(\mu\nabla v) - \frac{\partial P}{\partial y} + \frac{C^*\left(1-f_l^*\right)^2}{\left(f_l^*\right)^3}v \tag{9}$$

$$\frac{\partial(\rho w)}{\partial t} + \nabla\cdot(\rho\boldsymbol{u}w) = \nabla\cdot(\mu\nabla w) - \frac{\partial P}{\partial z} + \frac{C^*\left(1-f_l^*\right)^2}{\left(f_l^*\right)^3}w + \frac{\rho g\beta(h-h_{\text{ref}})}{c} \tag{10}$$

Here, $v$ and $w$ are the scalar components of $\boldsymbol{u}$ in the $y$ and $z$ directions. In the buoyancy source term of Eq. (10), the coefficient of thermal expansion for liquid jet fuel, $\beta$, is determined from temperature-dependent density values. Here $h_{\text{ref}}$ is the enthalpy corresponding

**Table 2 DSC and GC measurements for different jet fuel samples**

| Fuel | $T_L$, K (±0.5 K) | $T_H$ (±0.5 K) | $\Delta H$, J/kg (±200 J/kg) | $f_s$ | $\Delta H_e$, J/kg | $f_{n-\text{alkane}}$ total |
|---|---|---|---|---|---|---|
| JP-8 (F3804) | 215.2 | 221.2 | 4968 | 0.08 | 62100 | 0.238 |
| Jet A (F3219) | 217.2 | 222.2 | 3487 | 0.06 | 58117 | 0.187 |
| Jet A (F3219) + additive (F3607) | 213.4 | 221.6 | 3581 | 0.06 | 59683 | 0.187 |

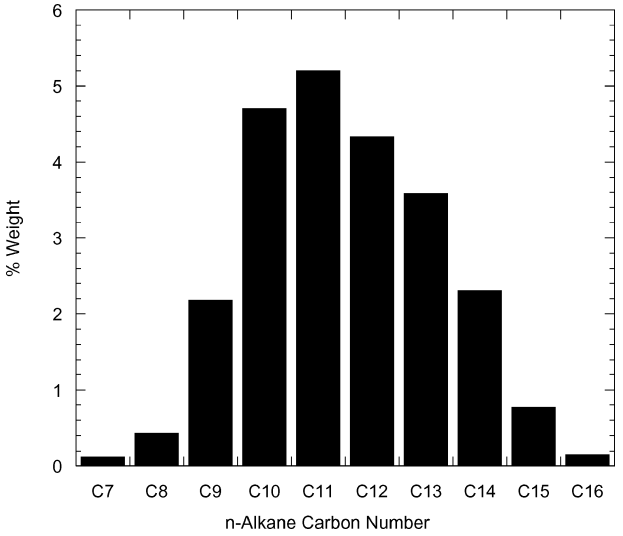


**Fig. 6 Measured distribution of *n*–alkanes for F3804 (JP-8).**

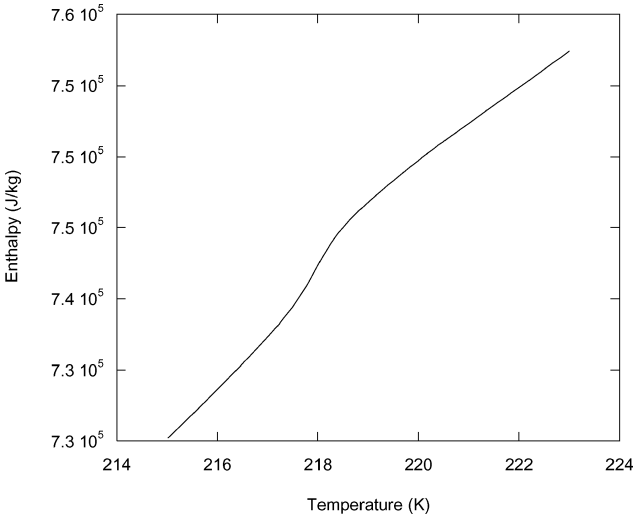


**Fig. 7 Derived enthalpy function for fuel sample F3804 (JP-8).**

to the lowest temperature achieved. In addition, the energy equation includes phase change and is written using $H$ of Eq. (1),

$$\frac{\partial(\rho H)}{\partial t} + \nabla \cdot (H\rho \boldsymbol{u}) - \nabla \cdot (k\nabla T) = 0 \tag{11}$$

Equations (9–11), along with the continuity equation (12), represent the system of coupled governing partial differential equations used.

$$\nabla \cdot \boldsymbol{u} = 0 \tag{12}$$

Figure 5 shows how DSC measurements can be used to determine enthalpy as a function of temperature, which also incorporates the heat of fusion. Measurements for F3804 show that the specific heat may be reasonably assumed to be a constant until the onset of freezing (221.2 K) and a different constant after freezing is essentially complete (215.2 K). A sigmoidal baseline is used to compensate for the change in baseline that occurs during phase change.[20] The specific heat can be numerically integrated to yield the temperature-dependent enthalpy for the mixture. Thus, the shaded area of Fig. 5 represents the heat of fusion ($\Delta H$) of precipitating *n*–alkanes under the solvent influence of the remaining hydrocarbon constituents. Because of the heat of fusion generated on cooling, the crystallization of large *n*–alkanes yields an exotherm measured by the DSC. Moreover, other fuel species, that is, isoparaffins, naphthenes, and aromatics, do not contribute significantly to this exotherm.[21] Figure 6 shows the measured *n*–alkane distribution for F3804 and that the fuel has an *n*–alkane mass fraction $f_{n-\text{alkane}}$ of 0.238. As already stated, less than one-third of these *n*–alkanes actually solidify at the temperatures of interest, resulting in a maximum solidifying mass fraction $f_s$ of 8%. The DSC measured heat of fusion is divided by $f_s$ to estimate an effective latent heat, $\Delta H_e$,

$$\Delta H_e = \Delta H / f_s \tag{13}$$

For the present JP-8 sample (F3804), the measured $\Delta H = 4968$ J/kg (shaded area, Fig. 5), and $\Delta H_e = 62{,}100$ J/kg [Eq. (13)]. Similar DSC and gas chromatography (GC) measurements were performed for the Jet A (F3219) sample and the Jet A sample containing 2000 mg/l of cold-flow additive F3607. These measurements are summarized in Table 2.

Although crystallization dynamics of jet fuels is not well understood, precipitating *n*–alkanes have been hypothesized to form a matrix that entraps other fuel species that remain in the liquid phase or possibly exist as a gel. Fuel cooled to the pour-point temperature does not flow and is, therefore, unavailable for use (referred to as fuel tank hold-up). Because the ability to predict the unavailable mass is important, the assumption that the fuel behaves as if it were essentially a nonflowing phase at 215.2 K is useful. $T_H$ and $T_L$ of Fig. 5 correlate well with the measured cloud- (onset of crystallization) and pour-point (gelation) temperatures, and this correlation suggests an approach to modeling. The enthalpy function of Fig. 7 was generated by numerical integration of the measured specific heat of Fig. 5. From $T_H$ to $T_L$, Fig. 7 shows that the enthalpy varies nearly linearly with temperature and that $f_l^*$ between $T_H$ and $T_L$ is estimated as

$$f_l^* = (T - T_L)/(T_H - T_L) \tag{14}$$

Thus, at temperatures above $T_H$, $f_l^*$ is one and, at temperatures below $T_L$, $f_l^*$ is zero.

## Numerical

A commercially available and modifiable CFD code, CFD-ACE was selected for use.[19] The program was modified to model solidification of mixtures as described here. An enthalpy formulation, fixed grid method was incorporated.[13] The temperatures at which solidification begins, $T_H$, and solidification ends, $T_L$, are required as input. Density, viscosity, thermal conductivity, and specific heat as functions of temperature are also required. The entire domain is considered porous with varying porosity to account for momentum resistance of porous solid–liquid regions, and $f_l^*$ is calculated. The program was also modified to accommodate the product of the morphology constant and viscosity, $C^*$.

CFD-ACE incorporates a finite volume approach using the SIMPLEC algorithm and offers a choice of spatial and temporal differencing options.[19] For the present simulations, the governing equations are represented by a blend of (0.9) third-order and (0.1) upwind

**Table 3 Grid refinement study for JP-8 at 1.0 K/min, $t = 3150$ s (values at optical cell center)**

| Grid size | Nodes | Cells | Temperature, K | $f_l$ | Temperature % change | $f_l$ % change | CPU time, *s* |
|---|---|---|---|---|---|---|---|
| 8 × 15 | 120 | 98 | 221.02 | 0.971 | — | — | 813.76 |
| 15 × 30 | 450 | 406 | 221.18 | 0.997 | 0.07 | 2.7 | 3411.37 |
| 21 × 42 | 900 | 820 | 221.23 | 1.000 | 0.02 | 0.3 | 7250.67 |
| 30 × 60 | 1800 | 1711 | 221.29 | 1.000 | 0.02 | 0.0 | 17998.95 |

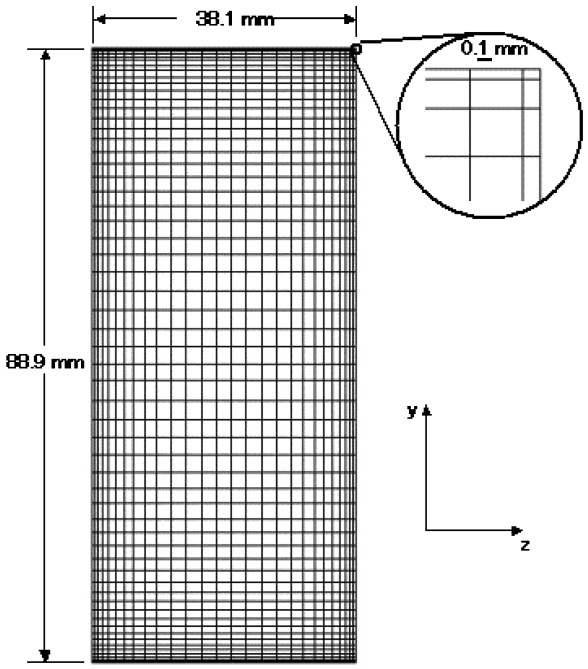


**Fig. 8 Structured grid.**

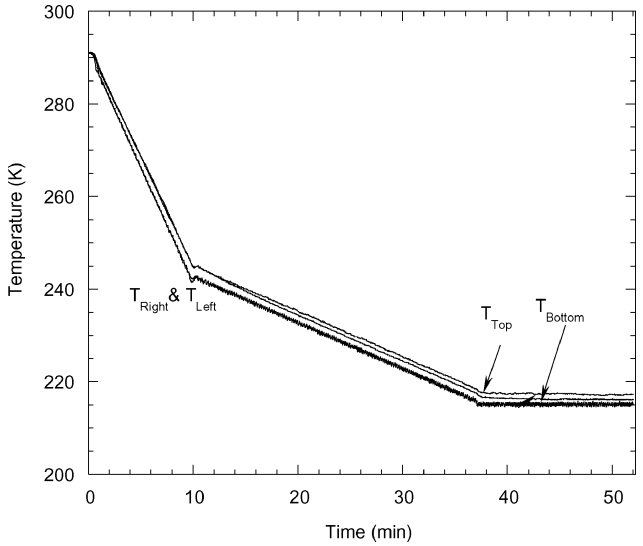


**Fig. 9 Measured surface temperatures applied as thermal boundary conditions for optical cell calculations for JP-8 fuel.**

spatial differencing. A Crank–Nicolson scheme is used for temporal differencing (see Ref. 19).

The rectangular computational domain used to represent the flow within the optical cell (Fig. 8) consists of a structured grid, clustered along each horizontal and vertical surface. The grid size and cluster spacing were determined after a grid refinement study for the neat JP-8 (F3804) fuel using the thermal boundary conditions of Fig. 9. The $f_l^*$ and temperature at the center of the computational domain were calculated for grid densities of 8 × 15, 15 × 30, 21 × 42, and

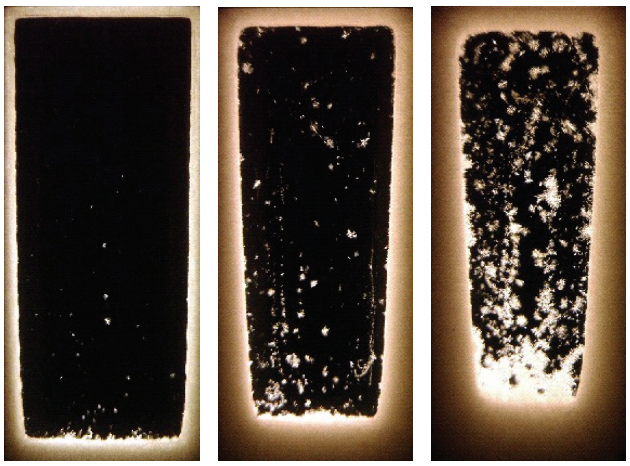


**Fig. 10 Solidifying JP-8 (F3804) in the optical cell after a) 37.5 min, b) 42.5 min, and c) 47.5 min of the applied thermal boundary conditions shown in Figure 9.**

30 × 60. A time step $\delta t$ of 1.0 s provided a stable solution and was small enough to resolve the unsteady convective motion for each grid density. The solution was considered complete for each time step if all variable residuals decreased by four orders of magnitude. A grid size of 30 × 60 was utilized based on the results of the grid refinement study (Table 3). The CPU (Pentium® III, 800 MHz) time for each solution is listed in Table 3 and shows a reasonable serial run time (approximately 5 h) for the selected grid. More complex geometries, such as actual aircraft wing tanks that include ribs and spars, may require a parallel computational solution to keep computational time manageable. The code selected is easily configured for parallel processing.

## Results and Discussion

### Simulations of the Solidification of JP-8

The JP-8 fuel sample (F3804) was subjected to the surface temperatures of Fig. 9. The vertical surfaces were cooled from room temperature at a rate of 5.0 K/min to 243.2 K to expedite the experiment by rapidly approaching the freeze-point temperature (224.9 K). The vertical surfaces were then more slowly cooled from 243.2 K to the pour-point temperature (215.2 K) at the desired rate of 1.0 K/min. The temperature of the optical cell vertical surfaces, $T_{\text{left}}$ and $T_{\text{right}}$, were maintained at 215.2 K for a period of 15 min to ensure adequate solidification. Images were obtained at 5-min intervals (37.5, 42.5, and 47.5 min). The top and bottom surface temperatures of the cell, $T_{\text{top}}$ and $T_{\text{bottom}}$, were not actively controlled, but were measured. The surface temperatures show in Fig. 9 were used as thermal boundary conditions in the simulations.

Figure 10 shows images of the JP-8 fuel sample obtained after 37.5, 42.5, and 47.5 min of cooling (Fig. 9). The use of cross polarized light eliminates light transmittance through liquid fuel, rendering images of the liquid as black regions. The formation of crystals depolarizes the light, and the crystals appear as the lightly colored regions. Figure 10 shows images of fuel solidifying on the cell surfaces and the liquid–solid region boundary advances symmetrically about the center axis of the cell. The symmetrical growth in time of the solidifying region is expected because of the symmetrical

thermal conditions (zero temperature difference between vertical surfaces).

Figure 10a shows the initial formation of free-floating crystals that drift within the liquid fuel. Figures 10b and 10c show that the number and size of these crystals increase with time. Similar behavior observed in metal alloy solidification research suggests that the origin of these crystals is nucleation within the liquid near a cool surface and dislodged or fractured adhered crystals.[3] On initial inspection, the number and size of these free-floating crystals appear to be significant in Fig. 10c. However, the optical cell is 44.5 mm in depth, and the actual number of crystals present in any single two-dimensional plane is significantly less than the cumulative image of Fig. 10c. Thus, momentum exchange between the liquid and free-floating crystals is neglected because the adhered structures are a more dominant effect. Finally, Fig. 10 shows that the crystallization behavior of the JP-8 sample is similar to that of the Jet A sample (F3219) presented in previous work.[7]

Because $C$ for the freezing of JP-8 and Jet A cannot be determined directly by crystal shape and size, $C^*$ is obtained by adjustment until agreement between the measured and simulated cell center temperature $T_{center}$ for a given fuel sample. (The simulated temperature at the center of the optical cell should be the same for any value of $C^*$ until the onset of solidification, 221.2 K for this JP-8 sample.) Figure 11 shows the measured temperature at the center of the optical cell, as well as the calculated temperature for three values of $C^*$. The measurement and simulation of the temperature at the cell center agree reasonably well (within 0.5 K) until solidification begins at 221.2 K. Once solidification begins, the solutions, which employ different $C^*$ values, begin to deviate due to the effect of flow through liquid–solid regions. With $C^* = 1$ kg/m$^3 \cdot$ s, the lowest $T_{center}$ is predicted. After 52.5 min, the predicted temperature is 218.1 K, which is 4.4 K below the measured temperature of 222.5 K. Figure 11 shows that a $C^*$ of $1 \times 10^6$ kg/m$^3 \cdot$ s increases the calculated $T_{center}$, and it more closely agrees with the measured temperature during solidification. Figure 11 shows that a $C^*$ of $1 \times 10^{10}$ kg/m$^3 \cdot$ s brings the simulated $T_{center}$ within 1.2 K (221.3 K predicted vs 222.5 K measured). Further increases in $C^*$ do not yield better predictions. Thus, a $C^* = 1 \times 10^{10}$ kg/m$^3 \cdot$ s was used in all JP-8 simulations. Figure 11 shows that relatively large values of $C^*$ are required for agreement between measured and simulated values of $T_{center}$.

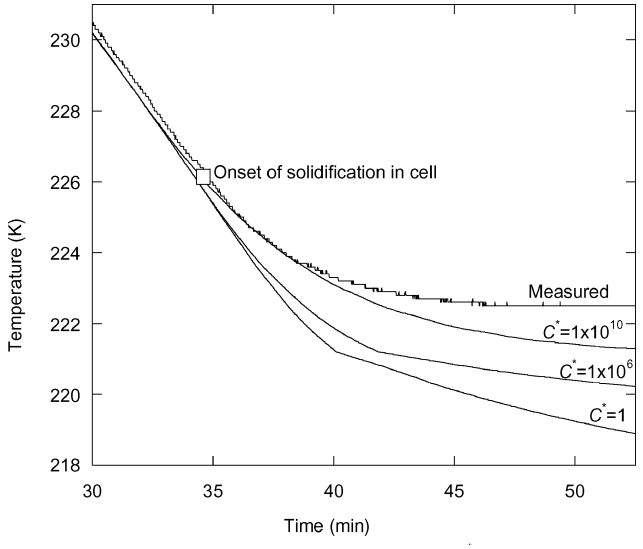


**Fig. 11 Predicted and measured $T_{center}$ for different values of $C^*$ for JP-8 sample (F3804).**

It is known that precipitating $n$–alkanes form a crystalline matrix or network about cooled liquid jet fuel, but the physical aspects of this liquid-entrapping mechanism are not well understood. Thus, it is important to conduct visualization studies involving simultaneous flow and crystallization. For reference, Fig. 12a shows a two-dimensional view of an entire face of the optical cell. Figure 12b shows a magnified image of crystal structures that have grown outward from the vertical cell surfaces. Indicated by an arrow, newly formed crystals extend into the bulk liquid fuel. Crystals near the cooled vertical surface are believed to be more closely packed than the newly formed crystals protruding from the edge of the solidifying area. Individual jet fuel crystals (Fig. 12c) have platelike branches that extend in three dimensions, and these platelike crystals have been described as having an orthorhombic structure.[5] As the jet fuel crystals nucleate and grow into the flowing thermal boundary layer due to temperature and concentration gradients, they accumulate in layers and appear to have a random orientation with respect to each other. Liquid surrounded by contacting crystals is then effectively trapped in localized regions because the crystal orientations inhibit flow in all directions. In the present experiments, gentle stirring of the liquid fuel does not disrupt the matrix. Elsewhere, the mass of the matrix structure in which the liquid and solid phases of fuel coexist was found to consist primarily of the liquid phase, and phase separation was achieved by physically disrupting the crystalline structure.[18]

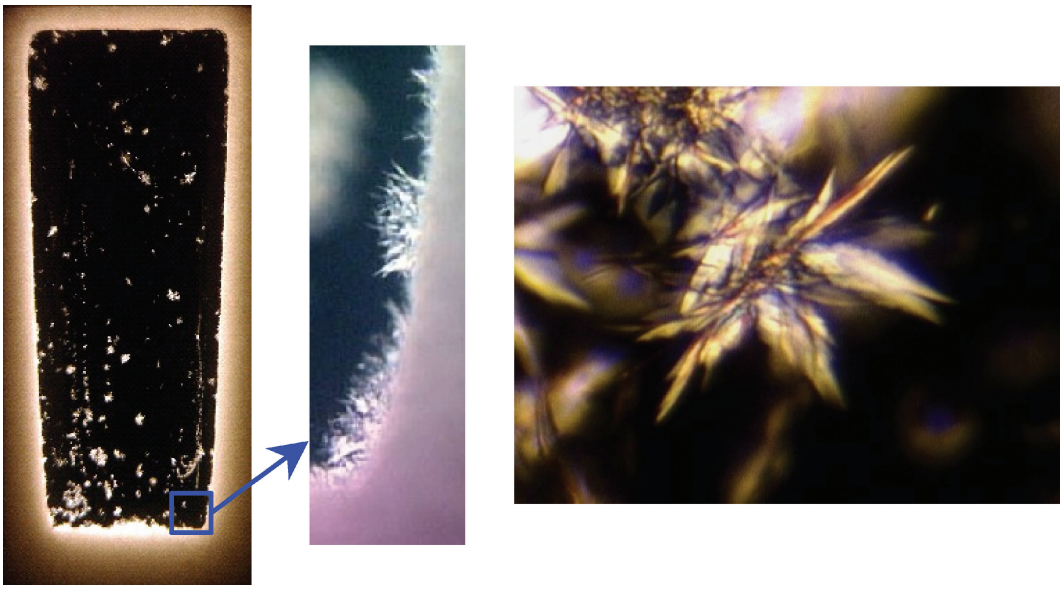


**Fig. 12 Solidifying JP-8 (F3804) in the optical cell after 47.5 min of applied thermal boundary conditions (Fig. 9); a) two-dimensional view of the cell, b) crystals on the advancing solidification front, and c) three-dimensional geometry of crystals with platelike branches.**

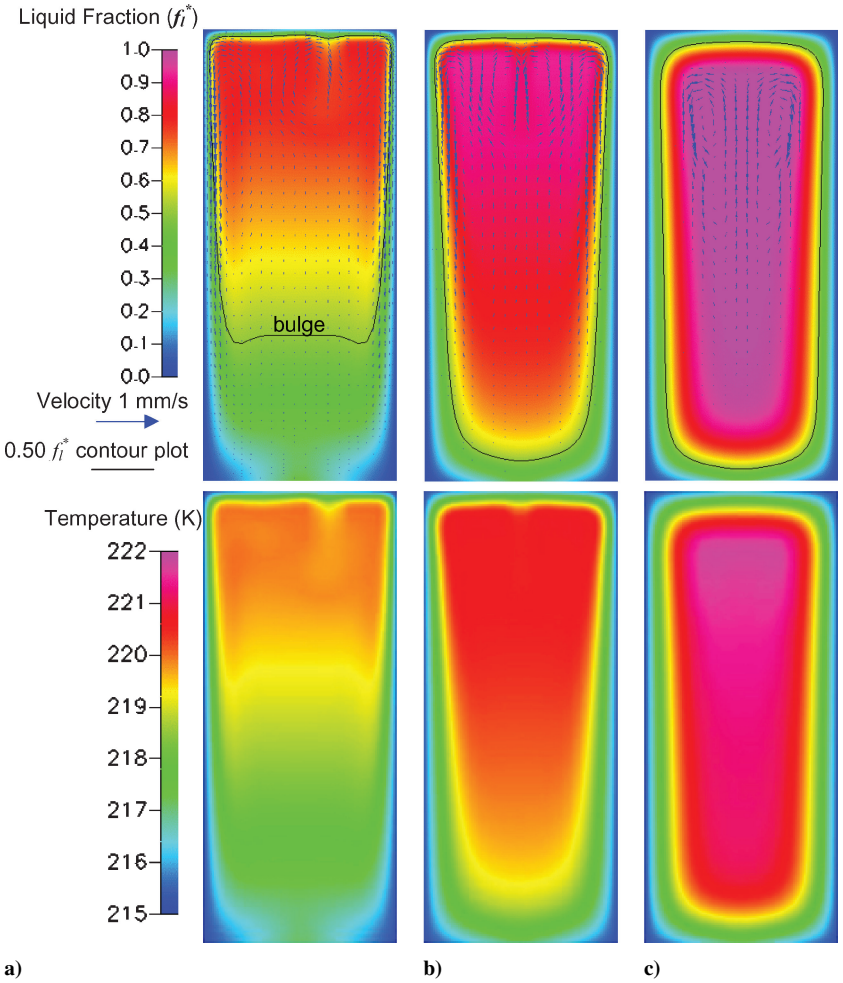


**Fig. 13 Simulated liquid fraction, velocity, and temperature for JP-8 after 52.5 min of the applied thermal boundary conditions of Fig. 9 for a) $C^* = 1$ kg/m$^3 \cdot$ s, b) $C^* = 1 \times 10^6$ kg/m$^3 \cdot$ s, and c) $C^* = 1 \times 10^{10}$ kg/m$^3 \cdot$ s.**

Although the value of $C^*$ in Eqs. (9) and (10) was selected by adjustment to match the temperature of the fuel at the center of the optical cell, it is important to understand the influence of $C^*$ on the flow velocity and solidification. Figure 13 shows simulations of JP-8 in the optical cell after 52.5 min for three values of $C^*$. Flood diagrams for simulated $f_l^*$, temperatures, and velocity vectors are presented. (For reference, an $f_l^*$ contour line of 0.5 is shown on the $f_l^*$ flood diagrams.) Figure 13a ($C^* = 1$ kg/m$^3 \cdot$ s) shows the lowest predicted $f_l^*$ (0.47) and $T_{\text{center}}$ (218.1 K) relative to Figs. 13b and 13c. In addition, Fig. 13a shows the greatest area of solidification. In Fig. 13a, the $f_l^*$ contour line of 0.5 has advanced from the lower portion of each vertical surface to the cell center. The protrusion or bulging of the solidifying structure is caused by significant flow in the porous liquid–solid region and is evident from the velocity vectors present there. Convection-induced bulges in liquid–solid regions have been observed in other studies of solidification within a cavity.[13] Relative to Figs. 13b and 13c, the low value of $C^*$ in Fig. 13a causes higher velocities in porous regions and the advancement of the solid region toward the cell center. Flow away from the colder lower regions on the vertical surfaces causes lower temperatures throughout the cell and overall greater solidification. Figure 13a shows the smallest area of solidification and highest temperatures to occur on the upper surfaces of the optical cell. Relatively warmer circulating fuel flow inhibits the growth of the solids on the upper surfaces.

Figure 13b shows simulations for $C^* = 1 \times 10^6$ kg/m$^3 \cdot$ s, and the velocity vectors show that less flow occurs in the liquid–solid regions relative to Fig. 13a. Consequently, reduced flow results in less heat transfer and higher temperatures throughout the cell. The temperature and $f_l^*$ at the cell center are 220.1 K and 0.81, respectively. The $0.50\,f_l^*$ contour of Fig. 13b encompasses a much larger area than that of Fig. 13a, extending to the bottom of the optical cell with no discernable convection bulge. Figure 13b shows much less solidification in the optical cell relative to Fig. 13a. However, more solidification occurs in the upper region of the optical cell because the larger value of $C^*$ reduces the heated return flow.

Figure 13c shows simulations for $C^* = 1 \times 10^{10}$ kg/m$^3 \cdot$ s. For this condition, the calculated temperature at the center of optical cell is 221.3 K, and $f_l^*$ is 1.0. The liquid fraction flood diagram shows that solidification has decreased overall. On the other hand, solidification has increased locally in the upper region of the optical cell. The velocity vectors show that flow has been substantially reduced in liquid–solid regions ($f_l^* < 1$). In addition, with this larger $C^*$ value, there is a symmetric pair of vortices that extend in the vertical direction over much of the optical cell and assist the circulation of fuel between the upper and lower regions of the cell.

Figure 13 demonstrates the effect of $C$ on the forming solidifying structures. The ability of freezing $n$–alkanes to trap liquid fuel and reduce buoyancy-driven flow (Fig. 12) is a behavior that will increase the magnitude of $C$ for jet fuel. From Eq. (9), larger $C^*$ values will reduce buoyancy-driven flow. As anticipated, Fig. 11 shows that the largest $C^*$ value better predicts temperature. Results from visualization should correspond, therefore, to simulations where $C^* = 1 \times 10^{10}$ kg/m$^3 \cdot$ s (Fig. 13c).

Simulations of jet fuel freezing are useful if they can predict fuel tank hold-up or the volume of jet fuel unavailable for use because of solidification. Thus, it is important to define what portion of the fuel in the optical cell essentially does not flow and is a part of the crystalline matrix. For the largest value of $C^*(1 \times 10^{10}$ kg/m$^3 \cdot$ s), Fig. 14 shows a comparison of simulated $f_l^*$ to the jet fuel after 37.5,

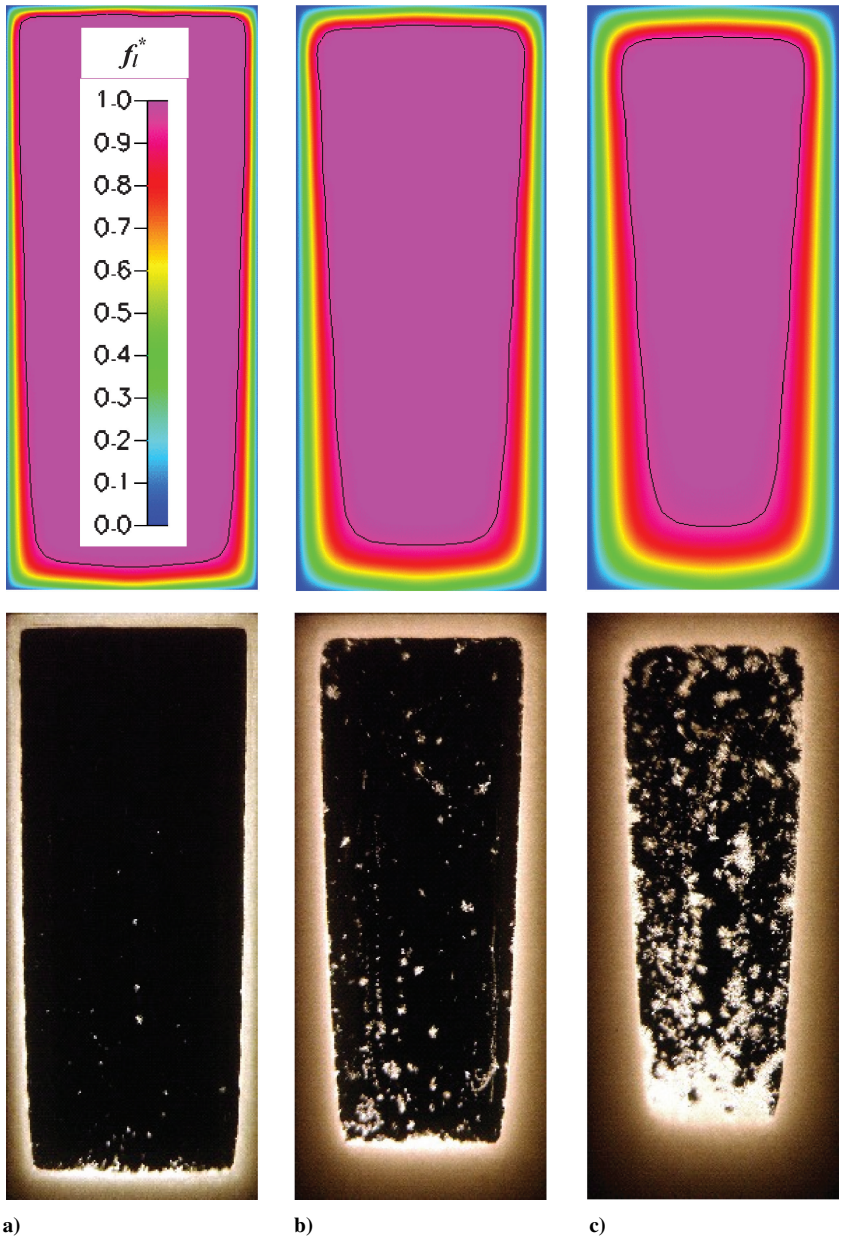


**Fig. 14 Predicted liquid fraction with $C^* = 1 \times 10^{10}$ kg/m$^3 \cdot$ s for images of JP-8 (F3804) after a) 37.5 min, b) 42.5 min, and c) 47.5 min of applied thermal boundary conditions of Figure 9. A black contour line representing an $f_l^*$ of 0.95 is shown for each condition.**

42.5, and 47.5 min of cooling. The simulations show an increase in the adhered liquid–solid structures with time as demonstrated by the decreasing liquid fraction and predicts the shape and area of the adhered structures. Figure 14 demonstrates that the model simulates the liquid–solid advancement reasonably well spatially and temporally. A black contour line representing an $f_l^* = 0.95$ is shown in Fig. 14 and demonstrates the ability of the model to predict the shape of the solidifying structure. The area of adhered solidified structure predicted by this contour line is 1704 mm$^2$. When the free-floating crystals and crystals that may settle by gravity on the bottom of the cell are neglected, the measured area of the two-phase region is 1680 mm$^2$. Thus, the use of a liquid fraction contour line with a value near unity provides a method to estimate the two-dimensional area of solid and entrapped liquid fuel.

#### Simulations of the Solidification of Jet A

The applicability of the current approach for use with various jet fuels is desirable because different jet fuels may have dissimilar low-temperature properties. Moreover, low-temperature properties of individual jet fuel samples of the same type (Jet A fuel or JP-8), may vary depending on the refinery source. Additional simulations were performed using properties of the Jet A fuel sample (F3219) and different thermal boundary conditions (Fig. 15). The use of other thermal boundary conditions can demonstrate the generality of the model. As with the JP-8 fuel sample, $C^*$ was adjusted until the measured $T_{\text{center}}$ agreed with the calculated value. As with the JP-8 fuel, Fig. 16 shows that a $C^*$ value of $1 \times 10^{10}$ kg/m$^3 \cdot$ s provides the optimum prediction of $T_{\text{center}}$ for the Jet A fuel. The model predicts the temperature to within 1.1 K of the measured temperature, which is similar to the accuracy of the JP-8 simulation shown in Fig. 11 (1.2 K). Figure 17 shows solidifying Jet A fuel (F3219) and that the crystal morphology and, thus, liquid fuel trapping mechanisms are similar to those of JP-8 (Figs. 10 and 12). Therefore, it is reasonable that the $C^*$ found for the JP-8 fuel sample would be of the same magnitude as the $C^*$ of the Jet A sample ($C^* = 1 \times 10^{10}$ kg/m$^3 \cdot$ s).

Figure 18a shows a flood diagram of simulated $f_l^*$ for the Jet A fuel sample using the measurements of Table 2. Figure 18b shows the image obtained from the optical cell for the same asymmetric thermal conditions used in the calculations. Figure 18a shows that a contour line corresponding to an $f_l^* = 0.95$ provides a good representation of the boundary between flowing liquid and the solid–liquid

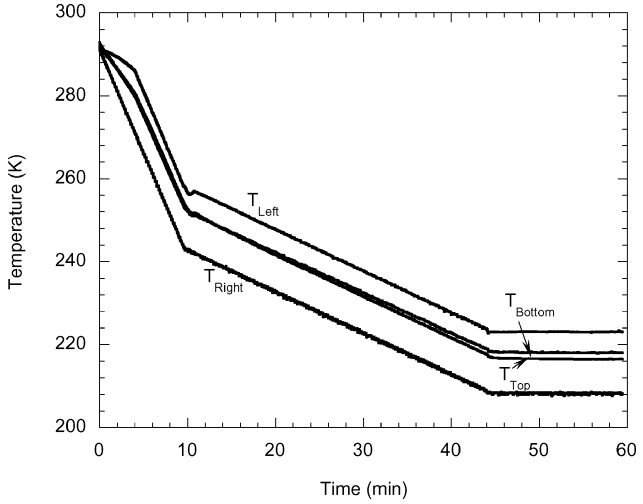


**Fig. 15 Thermal boundary conditions applied to the optical cell for Jet A (F3219).**

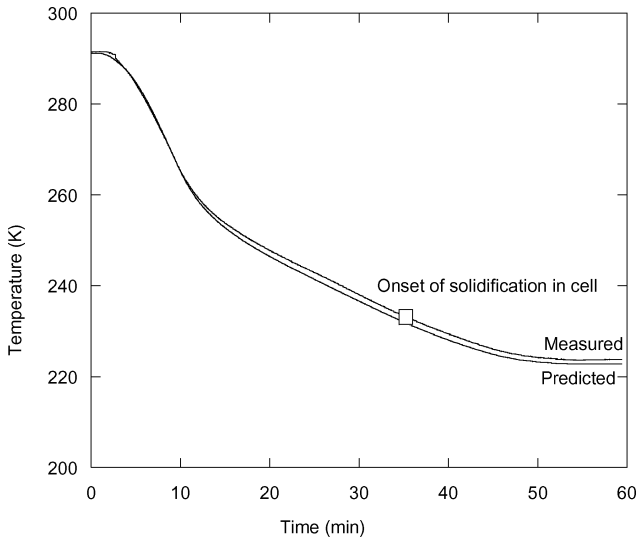


**Fig. 16 Calculated and measured $T_{center}$ for Jet A sample for a $C^*$ value of $1 \times 10^{10}$ kg/m$^3 \cdot$ s.**

regions, as with the JP-8 sample. Differences between the simulated and measured solidification on the left vertical surface of the optical cell (Figs. 18a and 18b) are likely due to the uncertainty in the measured surface boundary temperature and its proximity to the cloud-point temperature (222.2 K, Table 1). The area of adhered solidified structure enclosed by the $f_l^*$ contour line of 0.95 is 1039 mm$^2$, and this value agrees well with the measured area (947 mm$^2$) of the solidifying region. Figures 16 and 18 together show that the model can simulate reasonably well the freezing behavior of another fuel type.

### Simulations of the Freezing of Jet A Fuel Containing an Additive

There are potential commercial and military applications for developing additives to improve the low-temperature performance (reduced cloud point, increased flow ability) of Jet A and JP-8, fuels. Thus, it is desirable to simulate the freezing behavior of a jet fuel that contains a low-temperature additive. Here, the Jet A fuel sample is blended with 2000 mg/l of a proprietary additive (F3607), which has been observed to reduce the hold-up in large-scale tests. In experiments using a low-temperature microscope, the addition of the additive was found to change the platelike crystals of solidifying neat jet fuel into needlelike crystals.[22] In addition, the additive shifts the DSC peak associated with phase change of the Jet A sample to lower temperatures and lowers the cloud-point temperature by 0.6 K (Table 1).

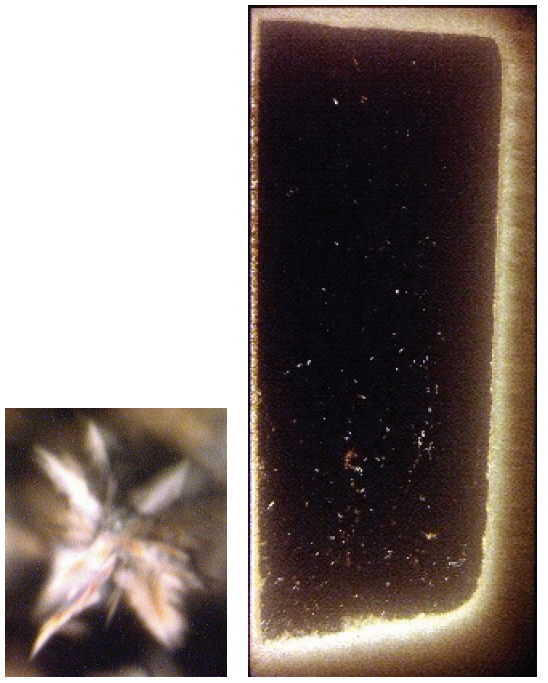

**a)** **b)**

**Fig. 17 Solidifying Jet A (F3219) after 50 min of applied thermal boundary conditions of Fig. 15: a) three-dimensional crystal geometry and b) two-dimensional view of the cell.**

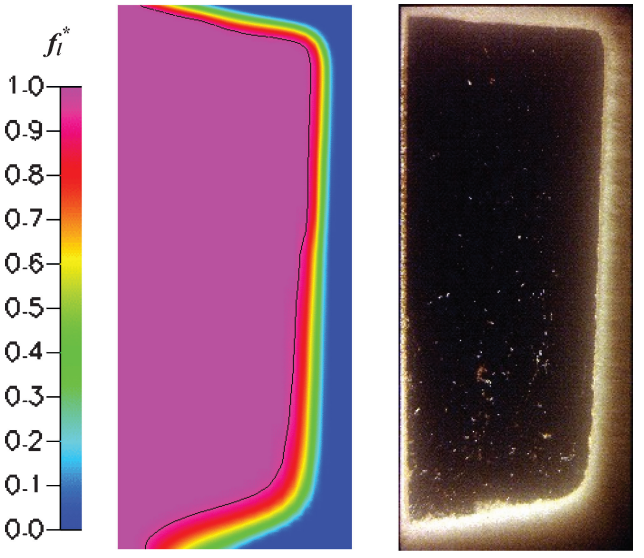


**a)** **b)**

**Fig. 18 Jet A (F3219) after 50 min of applied thermal boundary conditions of Fig. 15: a) flood diagram of simulated $f_l^*$ ($C^* = 1 \times 10^{10}$ kg/m$^3 \cdot$ s) with $f_l^*$ contour of 0.95 and b) image of Jet A.**

In previous work, it was observed that the solidification behavior of the fuel containing the additive is different from that of the neat Jet A fuel.[7] The fuel containing the additive tends to have smaller crystals, which do not pack in the same way as those observed in the case of the neat fuel. In contrast to the behavior of the neat fuel, stirring the liquid fuel easily disrupts the accumulation of crystals and allows them to flow into the bulk fuel. Figures 19a and 19b show simulations of $f_l^*$ for $C^*$ values of $1 \times 10^{10}$ and $1 \times 10^8$ kg/m$^3 \cdot$ s, respectively. Better agreement between the calculated and actual shape occurs with a $C^*$ value of $1 \times 10^8$ kg/m$^3 \cdot$ s. With this $C^*$ value, the calculated temperature at the center of the optical cell is within 3 K of the final measured value. The difference between the simulated and measured optical cell center temperatures for the fuel containing the additive is not as small as that for the neat fuels and

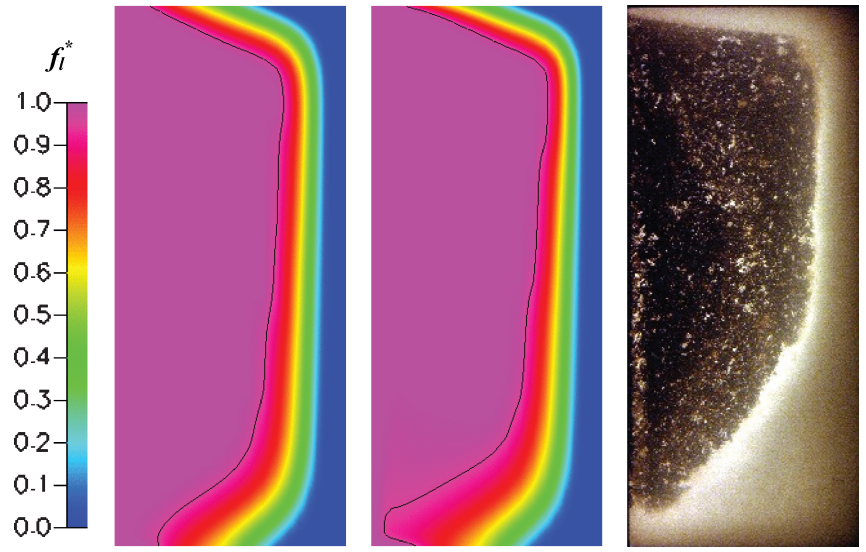


**Fig. 19 Solidification of Jet A (F3219) with 2000 mg/l of additive F3607 after 60 min of applied thermal conditions of Fig. 15; calculated $f_l^*$ for a) $C^* = 1 \times 10^{10}$ kg/m$^3 \cdot$ s and b) $C^* = 1 \times 10^8$ kg/m$^3 \cdot$ s and c) fuel. The black contour line represents an $f_l^*$ of 0.95.**

suggests that other mechanisms are involved. Further understanding of the behavior of classes of low-temperature additives is required to enable the application of the model to fuels containing additives.

#### Discussion of the Morphology Constant, $C$

A fundamental concern to be addressed is the interpretation of the constant $C$, used in the flow resistance term. $C$ represents the cumulative effects of $\Sigma$ together with the influence of pore geometry and orientation. The use of $C$ is a first step in simulating the freezing of jet fuel and permits reasonable simulations of $T_{\text{center}}$ and solidified areas. Note that the Jet A and JP-8 fuel samples had similar crystal morphologies, and the same value of $C^*(C\mu, 1 \times 10^{10}$ kg/m$^3 \cdot$ s) yielded acceptable simulations of the growth of the two-phase coexistence region. In addition, the fuel containing the additive formed crystals that were irregularly shaped and needlelike and did not readily trap liquid fuel. With regard to Eqs. (9) and (10), it is observed as $C^*$ is increased for a fixed $\lambda$ and velocity that the flow resistance increases. Thus, for the jet fuel containing the additive, a lower $C^*$ value ($1 \times 10^8$ kg/m$^3 \cdot$ s) might be anticipated. Indeed, a lower $C^*$ value was observed for the fuel containing the additive. Relatively large values of $C^*$ are shown here to be required for proper simulations. In simulations of metal alloy solidification, large $C$ values were also necessary.[13]

## Conclusions

A two-dimensional CFD model that reasonably predicts the solidification of jet fuels in a buoyancy-driven flow has been developed. The approach here uses DSC and GC measurements and enables the amount of hold-up due to fuel freezing to be estimated. Flow resistance caused by porous, adhered crystal structures was simulated using a momentum resistance source term. In addition, jet fuel properties were measured at low temperatures for use in the simulations. Optical cell flow-visualization experiments using polarized light enabled the measurement of areas of liquid–solid regions and the imaging of interactions between the flow and crystallization. The simulations agreed reasonably well with the solidified area and temperature measurements for the jet fuel samples and the thermal boundary conditions used. Thus, the current numerical model may be used as a tool by aircraft designers who need to predict fuel tank hold-up. The properties presented in the present work are specific to the fuels analyzed. Representative properties must be selected by the designer based on the level of model accuracy desired. The authors believe that the JP-8 sample utilized represents a freeze-point specification minimum fuel and the measured properties may potentially be used to predict the maximum hold-up.

The ability of solidifying jet fuel to entrap liquids was shown to minimize the buoyancy-driven flow through adhered solidifying crystalline structures. Trapped liquid is unlikely to flow due to buoyancy forces for both the Jet A and JP-8 samples. Comparisons between simulations and the visualization experiments demonstrated that buoyancy-driven flow was minimal in regions of adhered solidifying fuel. Simulations with additives show promise; however, predicted temperatures agree less with measured temperatures. Thus, further understanding of low-temperature additive behavior and refinement of the model are necessary for the additive application.

## Acknowledgments

This work was supported by the Dayton Area Graduate Studies Institute and the U.S. Air Force, Air Force Research Laboratory, Propulsion Directorate, Turbine Engines Division, Fuels Branch, Wright–Patterson Air Force Base, Ohio, under cooperative agreement F33615-03-2-2347. We would like to thank Marlin Vangsness and Linda Shafer for obtaining viscosity, density, and microscope images; Richard Striebich and Linda Shafer for obtaining gas chromatograph data; Nikki Widmor for obtaining differential scanning calorimeter data; and Kirsten Wohlwend (U.S. Air Force) and David Gollier for obtaining the freeze, pour, and cloud point temperature measurements.

## References

[1]McConnell, P. M., Owens, S. F., and Kamin, R. A., "Prediction of Fuel Freezing in Airplane Fuel Tanks of Arbitrary Geometry—Part 1," *Aircraft Engineering*, Vol. 58, No. 9, 1986, pp. 20–23.

[2]McConnell, P. M., Owens, S. F., and Kamin, R. A., "Prediction of Fuel Freezing in Airplane Fuel Tanks of Arbitrary Geometry—Part 2," *Aircraft Engineering*, Vol. 58, No. 10, 1986, pp. 2–7.

[3]Beckermann, C., and Viskanta, R., "Mathematical Modeling of Transport Phenomena During Alloy Solidification," *Applied Mechanical Review*, Vol. 46, No. 1, 1993, pp. 1–27.

[4]Desmarais, L. A., and Tolle, F. F., "Fuel Freeze Point Investigations," Air Force Research Lab., Technical Rept. AFWAL-TR-84-2049, Wright–Patterson Air Force Base, OH, July 1984.

[5]Coutinho, J. A. P., "A Thermodynamic Model for Predicting Wax Formation in Jet and Diesel Fuels," *Energy and Fuels*, Vol. 14, No. 3, 2000, pp. 625–631.

[6]Leo, A., and von Meerwall, E., "Fuel Holdup and Component Diffusivity in a Cooled Cylindrical Tank," *Journal of Aircraft*, Vol. 26, No. 5, 1989, pp. 465–469.

[7]Atkins, D. L., and Ervin, J. S., "Freezing of Jet Fuel within a Buoyancy-Driven Flow in a Rectangular Optical Cell," *Energy and Fuels*, Vol. 15, No. 5, 2001, pp. 1233–1240.

[8]"Handbook of Aviation Fuel Properties," Coordinating Research Council, Technical Rept. 530, Atlanta, GA, May 1988.

[9]Savant Independent Lubricant Testing and Research Lab., Midland, MI, June 2003.

[10]He, B., and Setterwall, F., "Technical Grade Paraffin Waxes as Phase Change Materials for Cool Thermal Storage and Cool Storage Systems Capital Cost Estimation," *Energy Conservation and Management*, Vol. 43, No. 13, 2002, pp. 1709–1723.

[11]"Thermal Conductivity of Liquid; Organic Compounds," Chemical Properties Handbook [online], URL: http://www.knovel.com [cited 2 March 2001].

[12]Yarbrough, D. W., and Kuan, C. E., "The Thermal Conductivity of Solid N–Eicosane, N–Octadecane, N–Heptadecane, N–Pentadecane, and N–Tetradecane," *Thermal Conductivity 17*, Plenum Press, New York, 1983, pp. 265–274.

[13]Voller, V. R., and Prakash, C., "A Fixed Grid Numerical Modeling Methodology for Convection–Diffusion Mushy Region Phase-Change Problems," *International Journal of Heat and Mass Transfer*, Vol. 30, No. 8, 1987, pp. 1709–1719.

[14]D'Arcy, H., *Les Fontainer Publiques de la Ville de Dijon*, Dalmont, Paris, 1856.

[15]Collins, R. E., *Flow of Fluids through Porous Materials*, Reinhold, New York, 1961, Chaps. 1–3.

[16]Kozeny, J. S., "Ueber kapillare Leitung des Wassers im Boden," *Sitzungsberichte, Akademie der Wissenschaften in Wien, Mathematisch-Naturwissenschaftliche Klasse*, Vol. 136, 1927, pp. 271–306.

[17]Carman, P., "Fluid Flow Through Granular Beds," *Transactions of the Institution of Chemical Engineers*, Vol. 15, May 1937, pp. 150–166.

[18]Moynihan, C. T., Mossadegh, R., and Bruce, A. J., "Determination of the Mass Fraction of Crystals in Partly Frozen Hydrocarbon Fuels," *Fuel*, Vol. 63, No. 3, March 1984, pp. 378–384.

[19]"CFD-ACE(U) Users Manual Version 2002," CFD Research Corporation, Huntsville, AL, March 2002.

[20]Wendlandt, W. W., *Thermal Analysis*; Wiley, New York, 1986.

[21]Zabarnick, S., and Widmor, N., "Studies of Jet Fuel Freezing by Differential Scanning Calorimetry," *Energy and Fuels*, Vol. 15, 2001, pp. 1447–1453.

[22]Widmor, N., Ervin, J. S., Zabarnick, S., and Vangsness, M., "Studies of Jet Fuel Freezing by Differential Scanning Calorimetry and Cold-Stage Microscopy," *Journal of Engineering for Gas Turbines and Power*, Vol. 125, No. 1, 2003, pp. 34–39.